Available online at www.sciencedirect.com

jmr&t Journal of Materials Research and Technology

journal homepage: www.elsevier.com/locate/jmrt

Original Article

Synthesis and additive manufacturing of calcium silicate hydrate scaffolds

Ezgi Ogur [a], *Renata Botti* [b], *Mauro Bortolotti* [c], *Paolo Colombo* [b], *Cekdar Vakifahmetoglu* [a,*]

[a] *Department of Materials Science and Engineering, Izmir Institute of Technology, Urla, Izmir, 35430, Turkey*
[b] *Dipartimento di Ingegneria Industriale, Università di Padova, Padova, 35131, Italy*
[c] *Dipartimento di Ingegneria Industriale, Università di Trento, Trento, 38123, Italy*

ARTICLE INFO

Article history:
Received 10 October 2020
Accepted 24 January 2021
Available online 30 January 2021

Keywords:
Calcium silicate hydrate
Xonotlite
Wollastonite
Hydrothermal
Additive manufacturing

ABSTRACT

A Calcium silicate hydrate (CSH) powder containing above 60 wt% xonotlite (remaining being tobermorite, scawtite and calcite) were produced from lime and ordinary recycled soda-lime glass via simple hydrothermal synthesis route. The thermogravimetric analysis demonstrated only ~20%weight loss up to 800 °C (at about the transformation temperature of CSHs to wollastonite), reaching a plateau in the 800–1200 °C temperature range. The synthesized CSH powder was employed for the fabrication of both green and heat-treated scaffolds by additive manufacturing (AM), possessing a high porosity (>80 vol%) and limited strength (~0.9 MPa).

1. Introduction

Calcium silicates (CSs) are a family of inorganic materials including mainly Ca, Si and O at different ratios, making wide variety of phases and chemical compositions including the OH bearing calcium silicate hydrates (CSHs) [1]. Both CS and CSH compounds find use in several sectors ranging from building industry [2] to healthcare [3] and to the refractory and nuclear industry [4,5].

The production of CSs can be carried out by a number of methods such as high temperature solid-

state reaction, co-precipitation, sol–gel, etc [6–8]. As know Portland cement is the most commonly used (billions of metric tons per year of consumption) man-made synthetic material. When cement "clinker" is blended with water, after complex reactions portlandite and CSHs including tobermorite and jennite forms [9]. These phases are actually the cement hydration compounds. For such important building material, there is an immense number of works towards the analysis of CSH phases, and its products [10].

Apart from cement derived CSHs, in order to synthesize individual CSHs, one may follow several pathways (like mechano-chemical [11] and emulsion processing [12]) but the majority of the studies was based on the hydrothermal techniques. For hydrothermal synthesis of CSHs, factors such as the raw materials (size, purity, surface area, etc. of the calcium

* Corresponding author.
E-mail addresses: cekdarvakifahmetoglu@iyte.edu.tr, cvahmetoglu@gmail.com (C. Vakifahmetoglu).
https://doi.org/10.1016/j.jmrt.2021.01.090

and silicon sources), water to solid ratio (W/S), temperature (T), time (t), Ca to Si molar ratio (Ca/Si), solution pH, and even the reactor type (i.e., if the autoclave is equipped with a stirrer or heater) play an important role in the quality of the final product [13–16]. When purity is a concern, generally silica (crystallized or amorphous), and CaO (from calcium carbonate, $CaCO_3$, calcination) have been used to provide silicon and calcium for the CSH synthesis, respectively [4,14]. Other works reported the use of blast furnace slag [17], K-feldspar [15], glass [13,18], carbide slag [19], clay bricks [20], $Na_2SiO_3 \cdot 9H_2O$, and $Ca(NO_3)_2 \cdot 4H_2O$ [21], etc. as reactants. Not only extent of the raw materials used but also reaction parameters can be varied in a wide range of values, e.g., the W/S ratio from 1.00 [22] to 115.00 [23], the reaction temperature from 60 °C [24] to 450 °C [25], and the reaction time from 2 h [26] up to 196 days [27] yielding various CSH phases.

For CSs and CSHs, the molar ratio of calcium to silicon (Ca/Si) is generally kept in between 0.5 and 3.0 [28]. While CSHs are the main cement hydration products, considering the hydrothermal synthesis of individual CSHs, it could be stated that the ones with a calcium to silicon molar ratio of 1, i.e., xonotlite ($Ca_6Si_6O_{17}(OH)_2$) and of ~0.83, i.e., tobermorite ($Ca_5Si_6O_{16}(OH)_2 \cdot 4H_2O$) are the most investigated ones [29]. This is because both xonotlite and tobermorite have good chemical and thermal durability. Heating in ambient air to temperatures around above 800 °C causes only a small weight loss and a conversion to higher stability CS mineral, known as wollastonite ($CaSiO_3$) [30]. As cast, porous (~70%) Xonotlite cylindrical monoliths had a rather good mechanical strength (7–15 MPa compression strength up to ~600 °C [14]), low thermal conductivity, e.g., a sample with 0.125 g cm^{-3} bulk density possessed a thermal conductivity of ~0.042 W m^{-1} K^{-1} [31], and high thermal shock resistance [32].

The morphology of the hydrothermally synthesized xonotlite is generally fibrous, and referred to as needle-like, acicular or nanobelt-like. While the morphology resembles that of asbestos fibers which occurs generally with a length below 100 μm and diameters ranging from 0.03 μm to 3.00 μm [33,34]), causing progressive diseases such as cancer [35], both xonotlite and tobermorite have been shown to be biocompatible [36,37]. All these properties, together with the ease of shaping into a porous structure due to the advantages offered by their inherent acicular morphology [38], make CSH a valuable material in the building industry, providing insulation and fire resistance/protection [19,32], in the automotive industry, as brake linings for thermal stability [39], and in the aerospace industry [32].

Previously by using DIW, tricalcium silicate/mesoporous bioactive glass (alite/MBG) components were fabricated to be used as a scaffold for bone regeneration (C_3S cement was synthesized by the sol–gel, followed by calcination) [40]. A similar study was also conducted using only alite [41]. For synthetic bone/tissue engineering applications, β-tricalcium phosphate (TCP) composites were also 3D printed [42]. In another investigation, diopside-based porous bioceramic composites were obtained by using magnesium substituted wollastonite as reinforcement [43]. In some of these examples, the printed log pile scaffolds were sintered at above 1100 °C for a few hours after manufacturing [42], except when a self-setting C_3S cement was employed [40,41].

In previous works, CSH powder synthesis and the properties of the synthesized powders were reported; however, there are there only a few studies focused on the fabrication of CSH monoliths [44], and in actual fact no studies, as far as the authors are aware, investigated the additive manufacturing (AM) of hydrated calcium silicates, excluding the cement based studies. Accordingly, the present work aims to hydrothermally synthesize CSHs starting from cost-effective raw materials, such as lime and recycled soda-lime glass. Then, employ the synthesized powder for the fabrication of 3D printed components for potential use as economic filters for wastewater, air purification and for sound & thermal insulation.

2. Experimental procedure

2.1. Synthesis

The CSH was synthesized by using recycled glass (provided by Sisecam, Turkey), having a chemical composition of 71.59 wt% SiO_2, 8.73 wt% CaO, 1.23 wt% Al_2O_3, 4.17 wt% MgO, 13.63 wt% Na_2O, and lime ($Ca(OH)_2$, TS-EN 459-1 CL 90 S, Nuh Kirec, Turkey), having a chemical composition of 90.9 wt% $Ca(OH)_2$, max 5 wt% MgO, max 2 wt% SO_3, max 2 wt% free water, max 4 wt.% loss on ignition, for both raw materials composition information was provided by the company sources. Deionized water (DI, Ultrapure Type-I, 18.2 MΩ cm at 25 °C) was obtained using a Millipak Direct-Q® 8 UV (Millipore, MA, USA) water purification system.

A planetary ball mill (PM-100, 250 mL, Retsch, Haan, Germany) was used for grinding and mixing the raw materials using agate balls and jar. An acid digestion vessel static autoclave (4748 model, Parr, Moline, IL, USA) was used for the hydrothermal synthesis. The prepared slurry was put into a PTFE Teflon® cup (125 mL) and reacted in the static autoclave. For the preparation of the slurry, lime and recycled glass (previously ground and sieved below 25 μm) were inserted in the grinding jar, keeping the Ca/Si molar ratio at 0.83. After 10 h of ball milling, additional DI water was added to make the final slurry volume below around 70 vol% of the autoclave liner volume, while keeping the water to solid ratio of 20. Following that, the liner was placed into the static autoclave and sealed for the hydrothermal process, performed at 220 °C for 20 h in an oven (UN55, Memmert GmBH + Co.KG, Germany). The obtained product was washed several times with DI water, filtered and dried in the oven at 90 °C. In additional experiments, the synthesized powder was also calcined for 2 h at 1000 °C with a 5 °C·min^{-1} heating rate, to obtain CS.

2.2. Additive manufacturing

Additive manufacturing was carried out by the Direct Ink Writing (DIW) technology using the as received synthesized CSH powder (94.24 wt.% on a dry basis), carboxymethyl cellulose (5.76 wt.% on dry basis) and water (~60 wt.%) as needed to obtain an optimized ink with the appropriate pseudoplastic behavior enabling the manufacture of lattices with suspended struts/trusses. For an optimum ink deposition, blends with different solid/water ratios (from 0.6 to 0.8) were tested. The

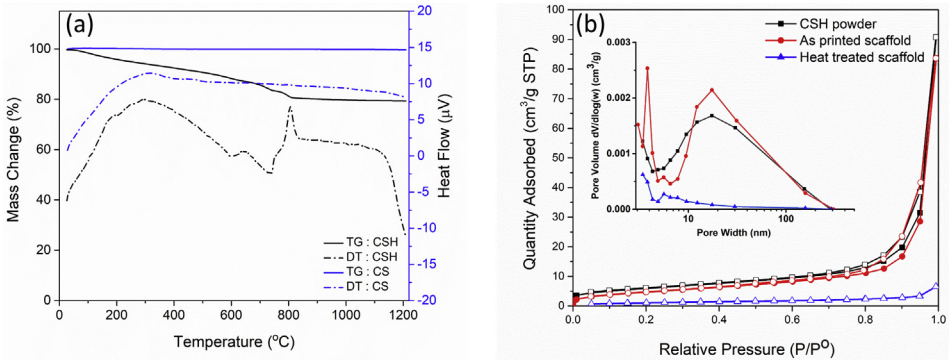

Fig. 1 – (a) TG-DTA of the synthesized CSH powder and the same sample after calcination (CS) at 1000 °C; (b) N_2 adsorption–desorption isotherms and pore size distribution (inset) for the synthesized powder, as printed green, and heat-treated scaffolds.

ratio of 0.68 which was then selected since it was strong enough to be extruded to form required lattices that retains its shape without the sagging of the filaments. The ink was printed using a delta printer (Delta Wasp 2040 Turbo, Wasproject, Massa Lombarda, IT) with gas transferring the mixture from a syringe to a pressurized vessel equipped with an infinite screw, extruding the material through a conical nozzle with diameter of 840 μm (Nordson Italia S. p.A.). The printing was carried out at room temperature (RT) in air, with a speed of 10 mm/s and an optimized flow rate. The fist layer was composed by filaments parallel to each other while the second layer was rotated by 90° from the previous layer, and this sequence was repeated until the lattice reached the desired height (log pile scaffold architecture). Square samples of 20 mm of length and width and 9.6 mm of height were printed and dried at RT for a week, followed by additional drying in an oven at 40 °C for one more week to ensure complete drying. As printed lattices were also heat treated for 1 h at 1000 °C/air, with a heating rate of 5 °C/min.

2.3. *Characterization*

Both the synthesized and calcined powder was analyzed by thermogravimetric analysis (TGA, Netzsch STA 409, Netzsch Geratebau Gmbh, Selb, Germany) up to 1200 °C in air, with a 5 °C/min heating rate. X-ray diffraction (XRD) measurements were performed on an instrument (Rigaku D-Max-B Tokyo, Japan) operating in Bragg–Brentano geometry and equipped with a copper target X-ray source (40 kV and 30 mA, Cu $K\alpha_{avg}$ = 1.54184 Å), a diffracted beam graphite monochromator, 1° divergence & 1° receiving slit and 5° diffracted beam Soller slits. Scans were performed over the 5–115° (2θ) range, with a 0.02° step size and 2s counting time per step. The morphological properties of the powder and the 3D printed scaffolds were analyzed by Scanning Electron Microscopy (SEM, Quanta 250, FEI, Hillsboro, OR, USA), and the surfaces were sputter coated prior to the imaging with a ~10 nm Au layer. ImageJ software was used to extract quantitative information from the SEM images, and the reported data are the average of at least 100 individual measurements. For transmission electron microscopy (TEM, 200 kV, ThermoFisher Talos F200S FEG, Netherlands) analysis, sample was prepared suspending a small amount of powder in ethanol, sonication, and placing a 50 μL of solution on a TEM copper grid covered by amorphous carbon.

Rheological tests were carried out to evaluate the suitability of the inks for DIW. A rotational rheometer (MCR 92, Anton Paar, Graz, Austria) equipped with 25 mm diameter parallel plates with a set temperature of 20 °C and a gap of 1 mm was used in the tests. The mechanical strength of the scaffolds was assessed by compression using a universal testing machine (Quasar 2.5, Galdabini 1890, Cardano al Campo, Italy), under a rate of 0.5 mm/min; 12 samples per type were tested, and the results are reported as average ± standard deviation. The bulk density was calculated considering the weight and volume of the lattices; true and apparent density of the samples were measured by helium pycnometer (Micromeritics AccuPyc 1330, Nor-cross, GA) using, respectively, finely powder and fragments of the scaffolds. The open and total porosity of the lattices was calculated as the ratio between their bulk and apparent density, and bulk and true density, respectively. The specific surface area (SSA) was determined by N_2 adsorption–desorption isotherms (Quantachrome Instruments, Boynton Beach, Florida, USA) using the multi-point Brunauer, Emmett, Teller (BET) method. The samples were degassed at 120 °C overnight; pore size distribution, average pore width and total pore volume were calculated from the desorption isotherm using the Barrett–Joyner–Halenda (BJH) method.

3. Results and discussion

According to the TG curve (see Fig. 1(a)), synthesized CSH sample had a total weight loss less than 20%. This value is reached at around 820 °C, and remained constant up to the final analysis temperature (1200 °C), due to the conversion of CSHs to wollastonite [32]. The DTA curve, given in Fig. 1(a), shows an exothermic peak at about 805 °C inferring that powder contained different types of CSHs, i.e., it was not comprised of phase pure xonotlite. This is because, xonotlite undergoes a topotactic transformation to wollastonite, and

does not show such sharp exothermic peak in the DTA around such temperatures [45]. On the other hand, it was shown that for xonotlite mixed with other CSHs (e.g., tobermorite), an exothermic peak at about 810 °C appears [44,46]. Such info was corroborated by the XRD data (see later) in accordance with the previous works [44,46]. It is clear from the TG/DTA data of the calcined powder (CS) that the formed material has enhanced thermal stability in air, demonstrating a very low weight loss (below 1 wt%) up to 1200 °C. However, the endothermic peak present at around 1150 °C may be attributed to decomposition, though it is known that β-Wollastonite is stable up to 1250 °C/air and transforms to α-Wollastonite then [47]. N_2 sorption analysis (see Fig. 1(b)) of the synthesized CSH powder resembles Type IV isotherm (IUPAC) with a hysteresis loop, implying a mesoporous (2–50 nm pores) nature. The specific surface area was around 21 m^2/g with an average pore size ranging from 10 to 100 nm (average being 17.46 nm) due probably to the interparticle porosity.

XRD analysis was performed following the Rietveld method using Maud [48,49]. Final Goodness of Fit (GOF) for the analysis was 1.31%, 1.31% and 1.36% for the CSH and CS sample analysis respectively; quantitative results relative to both samples are reported in Table 1, together with the fitting plots (see Fig. 2). According to the crystallographic phase quantification, the CSHs sample contained 60.73wt% Xonotlite (ICDD No. 23–0125), 9.81wt% Tobermorite (ICDD No. 86–2275), and 17.84 wt% Scawtite (ICDD No. 70–1279) as main phases. The average crystallite size was determined using an analytical isotropic size model [50,51]; and all the phases exhibited values around ~1000 Å, with the exception of the xonotlite, with values around ~500 Å. This may be due to the particular fibrous microstructure, as observed by SEM and TEM (see below). In some works, dealing with hydrothermally synthesized tobermorite [52,53], lower average crystallite size values ranging from 100 to 400 Å are reported, probably due to the adoption of the single-peak Scherrer approximation, for which the results should be treated as semi-quantitative at best even in ideal conditions (cubic symmetries and spherical crystallites [54]) and not considered reliable for low-symmetry crystallographic structures like tobermorite or xonotlite, especially in the case of complex non-spherical particle shapes. Indeed, a better agreement can be found when the full profile Rietveld modeling is adopted [55]. Preferred orientation effects were corrected with the standard functions model [56], in particular for tobermorite and xonotlite, and both phases exhibited a weak preferred orientation along the (001) crystallographic direction, again in reasonable agreement with their fibrous morphology.

Parallel analysis of the calcined sample showed, as expected, the dominant presence of dehydrated phases, being both pure calcium silicates as well as Mg and Na partially substituted compounds. For what regards the former, the presence of Wollastonite 2 M (ICDD No 43–1460) and Wollastonite 1 A (ICDD No 42–0547) was observed; both polymorphs belong to the low temperature stable β form, differing by crystal system and layer periodicity (monoclinic with 2-layer periodicity and triclinic with 1-layer periodicity for 2 M and 1 A respectively). In addition, a moderate amount of Dicalcium Silicate (ICDD No. 83–0460) was detected. Among the substituted CS compounds, Akermanite (ICDD No. 87–0046) and Combeite (ICDD No 78–1649) were found in considerable amount; the presence of Mg and Na bearing compounds can be justified by the composition of the raw materials, in particular alkali and alkaline earth oxides present in the recycled glass, similarly seen in other studies [57,58].

It has to be pointed out that, given the complexity of the phase mixture, the exact stoichiometry of these compounds cannot be accurately determined by the Rietveld modeling; indeed, substitutional changes in the crystallographic sites are reflected only by small positional shifts and intensity modifications of selected Bragg reflections (the latter being further affected by the aforementioned preferred orientation effects). Akermanite in particular, being an endmember of the Melilite solid solutions group (with the general formula $(Ca,Na)_2(Al,Mg)[(Al,Si)SiO_7]$), can as well be considered as a crystallographic placeholder for similar compounds with slightly different chemical composition. Finally, average crystallite sizes (evaluated again in the isotropic approximation) were significantly larger in comparison to the CSH sample, ranging between 2000 and 5000 Å; this is to be expected as a consequence of the thermal treatment, likely reducing lattice strains and defects of the crystallized phases.

Different CSH phases (α-C_2SH, CSH I & II, tobermorite, xonotlite, etc.) may be obtained depending on the reaction

Table 1 – The quantitative content of the phases and their average crystallite sizes in sample CSH and CS, as obtained from the Rietveld fitting.

Mineral Name	Formula	Weight (%)	Av. Cryst. Size (Å)
Hydrothermal synthesized powder			
Xonotlite	$Ca_6Si_6O_{17}(OH)_2$	60.73	532
Tobermorite	$Ca_5Si_6O_{16}(OH)_2 \cdot 4(H_2O)$	9.81	1152
Scawtite	$Ca_7Si_6O_{18}CO_3 \cdot 2(H_2O)$	17.84	908
Calcite	$CaCO_3$	2.58	1022
Vaterite	$CaCO_3$	9.04	927
Calcined powder			
Akermanite[a]	$Ca_2MgSi_2O_7$	30.04	2813
Wollastonite-2M	$CaSiO_3$	22.22	5184
Wollastonite-1A	$CaSiO_3$	11.01	2134
Combeite[a]	$Na_2Ca_2Si_3O_9$	22.71	2217
Larnite	Ca_2SiO_4	14.02	2000

[a] Approximate stoichiometry.

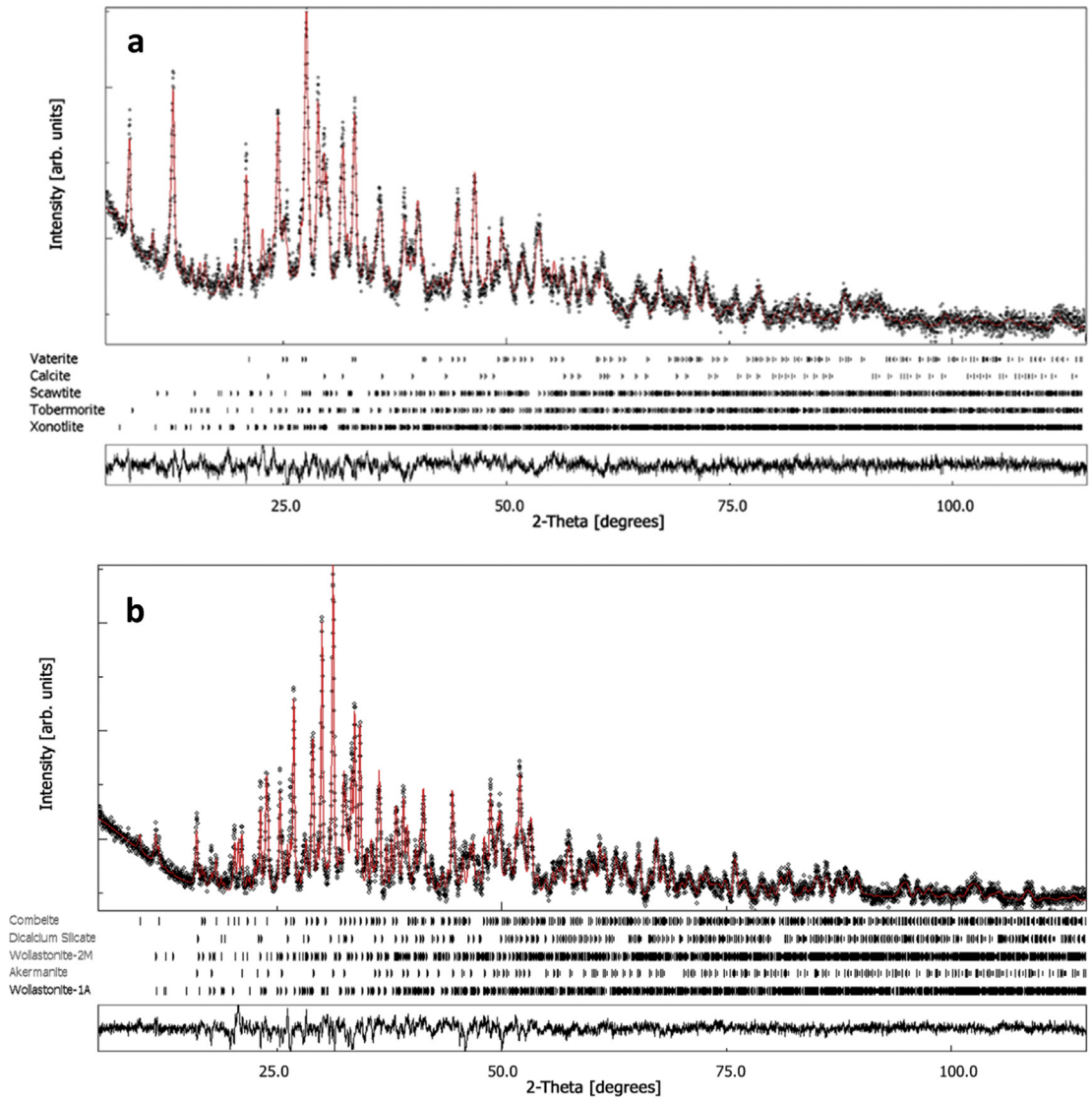

Fig. 2 – Rietveld fit of diffraction data collected on the (a) hydrothermally synthesized CSH powder, and (b) calcined sample. While experimental data is given with the straight black lines, calculated pattern is shown by red dots. The peak positions for probable phases are marked together with the residual fitting error plot given at the bottom of the pattern.

conditions and the Ca/Si ratio [59]. For example, when all other parameters are satisfied, tobermorite and xonotlite can be obtained from a Ca/Si molar ratio of 0.83–1. Reaction conditions should be strictly controlled to obtain single-phase CSH, but sill generally multi-phase CSH mixtures have been typically observed. For example, in a study where the Ca/Si ratio was fixed at 1 but simply the water/solids (W/S) ratio was modified from 15 to 10, the developed phases changed from phase pure xonotlite to a xonotlite-tobermorite mixture [46]. Although here no pure silicon or calcium sources but a recycled soda-lime glass containing various metal oxides were used for the synthesis, the selected reaction conditions were optimized to yield a powder with a high total amount (~90 wt.%) of CSHs, as demonstrated by the Rietveld analysis. As known hydrothermal reaction mechanisms and kinetics forming Ca-silicate hydrates are highly complex and include probable intermediate structure-controlling steps [60].

The SEM images of the synthesized CSH powder are given in Fig. 3(a-d). From the low magnification image given in Fig. 3(a), agglomerates resembling yarn-balls with a 100–300 μm diameter can be seen. When higher magnification images are examined (Fig. 3(b&c), it is seen that these agglomerates are mainly constituted by fibers with 9.81 ± 3.97 μm in length and 498 ± 257 nm in thickness, demonstrating a scale at least in one dimension it is below one micron. TEM image is given in Fig. 3(d) of the CSH together with the inset showing the complexity in the superposition of crystal symmetries, and the EDS analysis (data not shown)

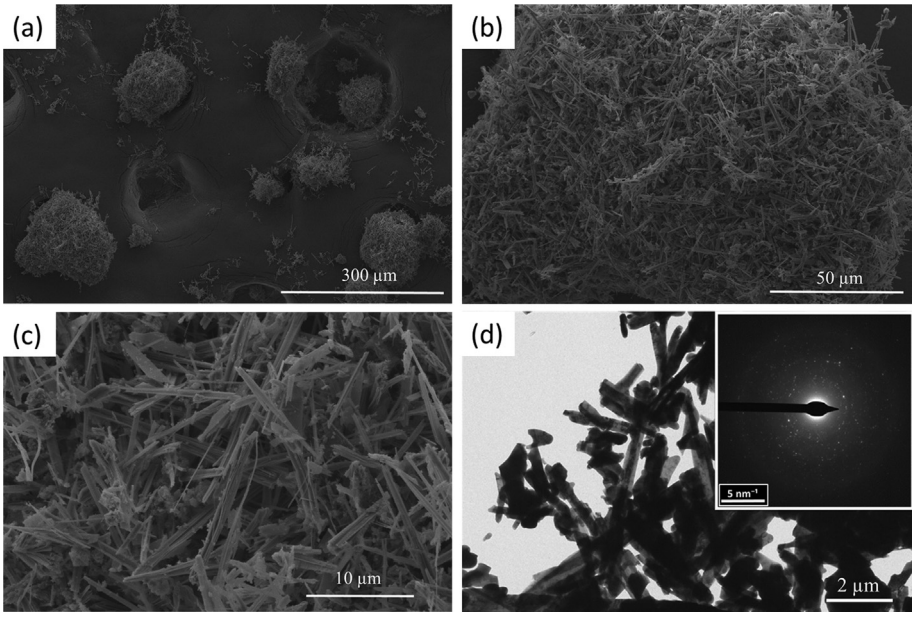

Fig. 3 – SEM images of the obtained CSHs powder; (a) general view showing few balls of yarn (note that the large holes in the background belong to the carbon tape) (b, c) higher magnification images showing details of the CSHs fibers; (d) TEM image of the CSH together with the; inset showing the complexity in the mixed crystals (symmetry point of view).

results showing Ca–Si–O with Mg (1.85 wt%) and Al (0.79 wt%) impurities most probably coming from the recycled glass. Since the signal statistic in the electron diffraction pattern is quite poor, it is not possible to exactly discriminate between the candidate crystallographic phases performing a crystal lattice indexing; however, it is still reasonable to ascribe acicular particle morphology to xonotlite and other CSH components, whereas the few plate-like particles can be attributed to minority higher symmetry phases (calcite and vaterite).

The rheology of the ink was extrapolated from the relation between the shear stress and the shear rate according to the three-parameter Herschel-Bulkley model: $\tau = \tau_0 + k\dot{\gamma}^n$ (where τ is the shear stress, $\dot{\gamma}$ is the shear rate, τ_0 is the yield stress, k is the consistency factor and n is the flow behavior index) [61], see Fig. 4. In particular, the flow behavior index quantifies the non-linear contribution to the stress response of a non-Newtonian fluid subjected to deformational flow. The yield stress quantifies the amount of stress that it is necessary to apply to the fluid in order to make it flow, while the consistency factor is a simple constant of proportionality. For the ink developed in this investigation, the values obtained from the fitting ($R^2 = 0.9922$) were: 16.22 kPa, 7.2 kPa·s^n, and n = 0.437 for the yield stress, the consistency factor and the flow behavior index, respectively. The value < 1 for the flow behavior index confirms the shear-thinning (pseudoplastic) behavior of the developed ink and therefore its suitability for printing structures possessing suspended struts.

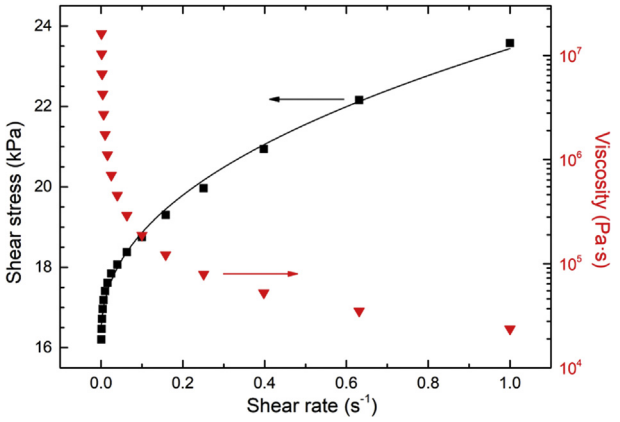

Fig. 4 – Shear stress and viscosity vs. shear rate for the developed ink. The continuous line is the fitting of the data according to the Herschel-Bulkley model ($R^2 = 0.9922$).

Table 2 reports the specific surface area (SSA), total pore volume, and average pore diameter data. As printed lattice had a SSA value of 16.08 m^2/g and in comparison, the starting CSH powder had only a slightly higher value of 20.64 m^2/g, indicating that the cellulose binder did not compromise the characteristics of the material, not-blocking the access of gas to the pores. The heat-treated lattice had a SSA value of 3.70 m^2/g, lower than that of the as printed lattice, implying sintering and shrinkage. Figure 1(b) show the N_2 sorption isotherms, and the pore size distribution of the samples (inset). Results demonstrated that both the synthesized powder and the as printed scaffold samples gave Type IV isotherms, characterizing the material still including mesoporosity after printing, with type H3 hysteresis loops, which are typically associated to non-rigid aggregates of plate-like particles or to the incomplete filling of macropores [62]. On the other hand, the heat-treated scaffold sample gave a reversible Type II isotherm, characteristic of the physisorption of gases on nonporous or macroporous materials.

Since the properties for AM formed similar CSH powders have not been yet covered in the literature, it is not easy to

Table 2 – N_2 sorption, relative density, and compressive strength of the printed scaffolds.

Sample	Mechanical Strength (MPa)	Total porosity (vol%)	Open porosity (vol%)	Specific surface area (m^2/g)	Total pore volume (cc/g)	Average pore diameter (nm)
CSHs powder	–	–	–	20.64	0.14	17.46
As printed scaffold	0.87 ± 0.36	81.68 ± 0.02	81.75 ± 0.02	16.08	0.13	3.82
Heat treated scaffold	0.11 ± 0.02	85.92 ± 0.02	85.91 ± 0.01	3.70	0.01	3.41

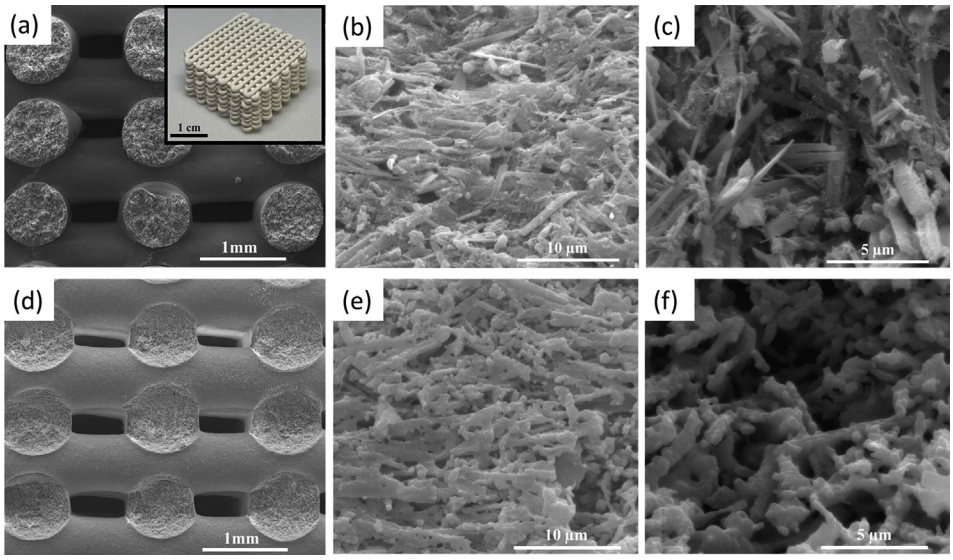

Fig. 5 – SEM images obtained from as printed green scaffold; (a) cross-section, the inset in the top-right corner shows the printed monolithic component; (b) external truss surface detail, (c) fractured (internal) truss detail, and from heat treated scaffold; (d) cross-section; (e) external truss surface detail, (f) fractured truss detail.

speculate on the mechanical strength, and the values given in Table 2, for the as printed and heat-treated scaffolds. The compression strength decreased from 0.87 ± 0.36 MPa for the as printed scaffolds to 0.11 ± 0.02 MPa for the heat treated samples at 1000 °C. Compared with xonotlite, tobermorite (and generally speaking other CSHs) develops larger shrinkage upon transforming to CS, resulting in significant reduction of the final mechanical properties [63]. In the same way here, there was a high reduction in the mechanical properties, and the total volumetric shrinkage measured was around 16%, i.e., much higher than those observed for the thermal transformation of pure xonotlite [64]. While further studies are needed to provide better understanding of strength reduction, such discrepancy can be related to a combination of some factors such as the increase in total porosity (to ~86 vol%, mostly open), the changes caused by the thermal transformation of the phases other than xonotlite, disappearance of cellulose binder aid available in the green state causing irregularities in between the layers, etc. It is important to note that for final component having an enhanced mechanical and thermal stability while pure xonotlite is therefore desired; remedies such as gypsum addition to the tobermorite could be considered [65].

The side sections of the scaffold (Fig. 5(a)) show the designed open channels between the layers in the Z-direction, with very limited deformation of the spanning filaments, indicating that the prepared ink had a suitable pseudoplastic behavior enabling the successful fabrication of unsupported features without sagging, corroborating rheology data given in Fig. 4. Upon firing, however, higher deformation occurred visible in the section detain given in Fig. 5(d). The external surface of the trusses for both as printed and the heat-treated samples are shown in Fig. 5(b & e) and instead in Fig. 5(c & f) the microstructures obtained from the fractured (internal) trusses are given.

It seems that the agglomerates (e.g., yarn-balls) presented in the CSH ink was no longer available, as the fibers appear to be oriented in the extrusion direction, due to the high shear stress in the nozzles during printing. The external truss surface is clearly less porous compared to that of the internal parts especially for the heat-treated sample. Around 22% of total weight loss was observed during heat treatment corroborating the TGA data together with the elimination of the cellulose binder. Besides, the fiber like morphology was retained after heat treating at 1000 °C, similar to other works, and the crystalline nature of the fibers is evident.

It should be pointed out that the resolution of the printed structure depends on several factors, including: a) rheology of the ink (how much it holds the shape after printing, which is related to the speed of recovery for the viscosity); b) specific

hardware (in the present case, x-y resolution is 15 μm and z resolution is 50 μmf, according to the manufacturer's specs); c) nozzle size (commercially available nozzles range from 60 microns to 2 mm).

4. Conclusions

The phase analysis of the hydrothermally synthesized powder demonstrated to be composed of different calcium silicate hydrates including majorly xonotlite and tobermorite together with scawtite and residual calcite. According to the thermal analysis, the CSH mixture had around 20% weight loss up to 820 °C, remaining constant up to 1200 °C. The obtained powder had a fibrous morphology entangled to form agglomerates similar to yarn-balls around 100–300 μm in diameter. These forms disappeared and fibers were oriented in the extrusion direction, due to shear stress in the nozzles during printing. While 3D printed green scaffolds showed around 80 vol% total porosity, 16 m^2/g specific surface area and a compressive strength reaching 0.9 MPa, heat treatment caused 22% weight loss, trusses with higher internal porosity and thus a reduction in the mechanical properties compared to that of the as printed scaffolds. The proposed process to form such scaffolds without heat treatment is in practical terms an implementation of eco-friendly glass recycling, and acquirement of profitable and efficient components that could be used for insulation and filtration applications.

Declaration of Competing Interest

The authors declare that they have no known competing financial interests or personal relationships that could have appeared to influence the work reported in this paper.

Acknowledgments

The author wishes to express sincere appreciation to Dr. Gloria Ischia from Department of Industrial Engineering, University of Trento, for TEM analysis. Cekdar Vakif Ahmetoglu acknowledges the support of the Alexander von Humboldt (AvH) Foundation.

REFERENCES

[1] Greenberg SA, Chang TN. Investigation of the colloidal hydrated calcium silicates. II. Solubility relationships in the calcium oxide-silica-water system at 25°. J Phys Chem 1965;69(1):182–8.
[2] Alawad OA, Alhozaimy A, Jaafar MS, Aziz FNA, Al-Negheimish A. Effect of autoclave curing on the microstructure of blended cement mixture incorporating ground dune sand and ground granulated blast furnace slag. Int J Concr Structures Mater 2015;9(3):381–90.
[3] Zhu Y-J, Guo X-X, Sham T-K. Calcium silicate-based drug delivery systems. Expet Opin Drug Deliv 2017;14(2):215–28.
[4] Yue H, Wang X, Yang Z, Wei C. Dynamic hydrothermal synthesis of super-low density xonotlite thermal insulation materials from industrial quartz powder. Key Eng Mater 2017;14(2):215–28.
[5] Glasser FP, Macphee DE, Lachowski EE. Solubility modelling of cements: implications for radioactive waste immobilisation. MRS Proc 2011;84:331.
[6] Leite FHG, Almeida TF, Faria RT, Holanda JNF. Synthesis and characterization of calcium silicate insulating material using avian eggshell waste. Ceram Int 2017;43(5):4674–9.
[7] Khristov TI, Popovich N, Galaktionov S, Soshchin N. Calcium silicate phosphors obtained by the sol-gel method. Glass Ceram 1994;51(9–10):290–6.
[8] Dhoble S, Dhoble N, Pode R. Preparation and characterization of Eu 3+ activated CaSiO3,(CaA)SiO3 [A= Ba or Sr] phosphors. Bull Mater Sci 2003;26(4):377–82.
[9] Dijkstra JJ, Comans RNJ, Schokker J, van der Meulen MJ. The geological significance of novel anthropogenic materials: deposits of industrial waste and by-products. Anthropocene 2019;28:100229.
[10] Giraudo N, Bergdolt S, Laye F, Krolla P, Lahann J, Thissen P. Dehydration and dehydroxylation of C-S-H phases synthesized on silicon wafers. Appl Surf Sci 2018;433:589–95.
[11] Black L, Garbev K, Stumm A. Structure, bonding and morphology of hydrothermally synthesised xonotlite. Adv Appl Ceram 2009;108(3):137–44.
[12] Lin K, Chang J, Lu J. Synthesis of wollastonite nanowires via hydrothermal microemulsion methods. Mater Lett 2006;60(24):3007–10.
[13] Tränkle S, Jahn D, Neumann T, Nicoleau L, Hüsing N, Volkmer D. Conventional and microwave assisted hydrothermal syntheses of 11 Å tobermorite. J Mater Chem 2013;1(35):10318–26.
[14] Milestone N, Ahari GK. Hydrothermal processing of xonotlite based compositions. Adv Appl Ceram 2007;106(6):302–8.
[15] Yang J, Tan X, Ma H, Zeng C, Peng H. Alkali-hydrothermal synthesis of acicular tobermorite using natural mineral K-feldspar powder. Ferroelectrics 2015;481(1):57–63.
[16] Liu F, Zeng LK, Cao JX, Zhu B, Yuan A. Hydrothermal synthesis of xonotlite fibers and investigation on their thermal property. Adv Mater Res 2010;105–106:841–3.
[17] Nakahira A, Naganuma H, Kubo T, Yamasaki Y. Synthesis of monolithic tobermorite from blast furnace slag and evaluation of its Pb removal ability. J Ceram Soc Jpn 2008;116(1351):500–4.
[18] Coleman NJ, Li Q, Raza A. Synthesis, structure and performance of calcium silicate ion exchangers from recycled container glass. Physicochem Probl Miner Process 2014;50:5–16.
[19] Liu F, Zeng L, Cao J, Li J. Preparation of ultra-light xonotlite thermal insulation material using carbide slag. J Wuhan Univ Technol -Materials Sci Ed 2010;25(2):295–7.
[20] Connan H, Ray A, Thomas P. Autoclaved lime-colloidal silica slurries and formation of tobermorite. J Australas Ceram Soc 2007;43:150–3.
[21] Wu J, Zhu Y-J, Cheng G-F, Huang Y-H. Microwave-assisted preparation of Ca6Si6O17 (OH)2 and β-CaSiO3 nanobelts. Mater Res Bull 2010;45(4):509–12.
[22] Hamid S. Electron microscopic characterization of the hydrothermal growth of synthetic 11Åtobermorite (Ca6Si6O18·4H2O crystals. J Cryst Growth 1979;46(3):421–6.
[23] Monasterio M, Gaitero JJ, Manzano H, Dolado JS, Cerveny S. Effect of chemical environment on the dynamics of water confined in calcium silicate minerals: natural and synthetic tobermorite. Langmuir 2015;31(17):4964–72.
[24] Hara N, Chan C, Mitsuda T. Formation of 14 Å tobermorite. Cement Concr Res 1978;8(1):113–5.

[25] Flint EP, McMurdie HF, Wells LS. Formation of hydrated calcium silicates at elevated temperatures and pressures. J Res Natl Bur Stand 1938;21(1):617–38.
[26] Yazdani A, Rezaie HR, Ghassai H. Investigation of hydrothermal synthesis of wollastonite using silica and nano silica at different pressures. J Ceram Process Res 2010;11(3):348–53.
[27] Speakman K. The stability of tobermorite in the system CaO-SiO 2-H 2 O at elevated temperatures and pressures. Mineral Mag J Mineral Soc 1968;36(284):1090–103.
[28] Richardson I. The calcium silicate hydrates. Cement Concr Res 2008;38(2):137–58.
[29] Shaw S, Clark S, Henderson C. Hydrothermal formation of the calcium silicate hydrates, tobermorite (Ca5Si6O16(OH)2· 4H2O) and xonotlite (Ca6Si6O17(OH)2): an in situ synchrotron study. Chem Geol 2000;167(1):129–40.
[30] Taylor HFW. 33. Hydrated calcium silicates. Part V. The water content of calcium silicate hydrate (I). J Chem Soc 1953:163–71.
[31] Wei G, Zhang X, Yu F. Thermal conductivity of xonotlite insulation material. Int J Thermophys 2007;28(5):1718–29.
[32] Levinskas R, Lukošiūtė I, Baltušnikas A, Kuoga A, Luobikienė A, Rodriguez J, et al. Modified xonotlite–type calcium silicate hydrate slabs for fire doors. J Fire Sci 2018;36(2):83–96.
[33] Moalli PA, MacDonald JL, Goodglick LA, Kane AB. Acute injury and regeneration of the mesothelium in response to asbestos fibers. Am J Pathol 1987;128(3):426–45.
[34] Suzuki Y, Yuen SR. Asbestos fibers contributing to the induction of human malignant mesothelioma. Ann NY Acad Sci 2002;982(1):160–76.
[35] Mossman BT, Kamp DW, Weitzman SA. Mechanisms of carcinogenesis and clinical features of asbestos-associated cancers. Canc Invest 1996;14(5):466–80.
[36] Lin K, Chang J, Cheng R. In vitro hydroxyapatite forming ability and dissolution of tobermorite nanofibers. Acta Biomater 2007;3(2):271–6.
[37] Bellmann B, Muhle H. Investigation of the biodurability of wollastonite and xonotlite. Environ Health Perspect 1994;102(suppl 5):191–5.
[38] Vakifahmetoglu C, Semerci T, Soraru GD. Closed porosity ceramics and glasses. J Am Ceram Soc 2019;103(5):2941–69.
[39] Anton O, Eckert A, Eckert A. Brake linings. Google Patents; 1991.
[40] Pei P, Qi X, Du X, Zhu M, Zhao S, Zhu Y. Three-dimensional printing of tricalcium silicate/mesoporous bioactive glass cement scaffolds for bone regeneration. J Mater Chem B 2016;4(46):7452–63.
[41] Yang C, Wang X, Ma B, Zhu H, Huan Z, Ma N, et al. 3D-Printed bioactive Ca3SiO5 bone cement scaffolds with nano surface structure for bone regeneration. ACS Appl Mater Interfaces 2017;9(7):5757–67.
[42] Deng Y, Jiang C, Li C, Li T, Peng M, Wang J, et al. 3D printed scaffolds of calcium silicate-doped β-TCP synergize with co-cultured endothelial and stromal cells to promote vascularization and bone formation. Sci Rep 2017;7(1):5588.
[43] He D, Zhuang C, Xu S, Ke X, Yang X, Zhang L, et al. 3D printing of Mg-substituted wollastonite reinforcing diopside porous bioceramics with enhanced mechanical and biological performances. Bioact Mater 2016;1(1):85–92.
[44] Vakifahmetoglu C. Zeolite decorated highly porous acicular calcium silicate ceramics. Ceram Int 2014;40(8, Part A):11925–32.
[45] Kalousek G, Mitsuda T, Taylor H. Xonotlite: cell parameters, thermogravimetry and analytical electron microscopy. Cement Concr Res 1977;7(3):305–12.
[46] Spudulis E, Šavareika V, Špokauskas A. Influence of hydrothermal synthesis condition on xonotlite crystal morphology. Mater Sci 2013;19(2):190–6.
[47] Núñez-Rodríguez LA, Tiburcio-Munive GC, Valenzuela-García JL, Gómez-Álvarez A, Encinas-Romero MA. Evaluation of bioactive properties of α and β wollastonite bioceramics soaked in a simulated body fluid. J Biomaterials Nanobiotechnol 2018;9(3):720–6.
[48] Paufler P, Young RA, editors. The Rietveld method. International union of crystallography. Oxford University Press; 1993. p. 298. Price £ 45.00. ISBN 0–19–855577–6. Cryst Res Technol. 1995;30(4):494-494.
[49] Bortolotti M, Lutterotti L, Pepponi G. Combining XRD and XRF analysis in one Rietveld-like fitting. Powder Diffr 2017;32(S1):S225–30.
[50] Popa N, Balzar D. An analytical approximation for a size-broadened profile given by the lognormal and gamma distributions. J Appl Crystallogr 2002;35(3):338–46.
[51] Delhez R, Keijser TH, Mittemeijer E. Determination of crystallite size and lattice distortions through X-ray diffraction line profile analysis. Z für Anal Chem 1982;312(1):1–16.
[52] Wang S, Peng X, Tang L, Zeng L, Lan C. Influence of hydrothermal synthesis conditions on the formation of calcium silicate hydrates: from amorphous to crystalline phases. J Wuhan Univ Technol -Materials Sci Ed 2018;33(5):1150–8.
[53] Saito T, Sakai E, Morioka M, Daimon M. Carbonation reaction of calcium silicate hydrates by hydrothermal synthesis at 150 C in OPC-γ-Ca2SiO4-α-quartz systems. J Adv Concr Technol 2007;5(3):333–41.
[54] Balzar D, Popović S. Reliability of the simplified integral-breadth methods in diffraction line-broadening analysis. J Appl Crystallogr 1996;29(1):16–23.
[55] Qu X, Zhao Z, Zhao X. Microstructure and characterization of aluminum-incorporated calcium silicate hydrates (C–S–H) under hydrothermal conditions. RSC Adv 2018;8(49):28198–208.
[56] Matthies S. Standard functions in the texture analysis. Phys Status Solidi 1980;101(2):K111–5.
[57] Bernardo E, Bonomo E, Dattoli A. Optimisation of sintered glass–ceramics from an industrial waste glass. Ceram Int 2010;36(5):1675–80.
[58] Bernardo E, Bingham PA. Sintered silicophosphate glass ceramics from MBM ash and recycled soda–lime–silica glass. Adv Appl Ceram 2011;110(1):41–8.
[59] Hartmann A, Schulenberg D, Buhl J-C. Synthesis and structural characterization of CSH-phases in the range of C/S= 0.41-1.66 at temperatures of the tobermorite xonotlite crossover. J Mater Sci Chem Eng 2015;3(11):39–55.
[60] Houston JR, Maxwell RS, Carroll SA. Transformation of meta-stable calcium silicate hydrates to tobermorite: reaction kinetics and molecular structure from XRD and NMR spectroscopy. Geochem Trans 2009;10:1–14.
[61] Rao MA. Flow and functional models for rheological properties of fluid foods. In: Rao MA, editor. Rheology of fluid, semisolid, and solid foods: principles and applications. Boston, MA: Springer US; 2014. p. 27–61.
[62] Thommes M, Kaneko K, Neimark AV, Olivier JP, Rodriguez-Reinoso F, Rouquerol J, et al. Physisorption of gases, with special reference to the evaluation of surface area and pore size distribution (IUPAC Technical Report). Pure Appl Chem 2015;87(9–10):1051–69.
[63] Pugovkina Y, Kutugin V, Ostroumova A, Rymanova I. High temperature and heat insulated calcium silicate materials. Key Eng Mater 2016;683:209–14.

[64] Lee C-K, Han S-M. The thermal transformation of xonotlite -studies on the thermal transformation of calcium silicate hydrates (I). J Korean Ceram Soc 1974;11(4):119–24.

[65] Yanagisawa K, Zhu K, Onda A, Kajiyoshi K, Kori T, Feng Q. Decrease of thermal shrinkage of tobermorite compacts at high temperatures by addition of gypsum. J Soc Inorg Mater Jpn 2003;10(307):363–9.